ORIGINAL PAPER

Quantitative Raman spectroscopy in turbid matter: reflection or transmission mode?

Dieter Oelkrug · Edwin Ostertag · Rudolf W. Kessler

Abstract Raman intensities from reflection (X_R) and transmission (X_T) setups are compared by calculations based on random walk and analytical approaches with respect to sample thickness, absorption, and scattering. Experiments incorporating strongly scattering organic polymer layers and powder tablets of pharmaceutical ingredients validate the theoretical findings. For nonabsorbing layers, the Raman reflection and transmission intensities rise steadily with the layer thickness, starting for very thin layers with the ratio $X_T/X_R=1$ and approaching for thick layers, a lower limit of $X_T/X_R=0.5$. This result is completely different from the primary irradiation where the ratio of transmittance/reflectance decays hyperbolically with the layer thickness to zero. In absorbing materials, X_R saturates at levels that depend strongly on the absorption and scattering coefficients. X_T passes through a maximum and decreases then exponentially with increasing layer thickness to zero. From the calculated radial intensity spreads, it follows that quantitative transmission Raman spectroscopy requires diameters of the detected sample areas be about six times larger than the sample thickness. In stratified systems, Raman transmission allows deep probing even of small quantities in buried layers. In double layers, the information is independent from the side of the measurements. In triple layers simulating coated tablets, the information of X_T originates mainly from the center of the bulk material whereas X_R highlights the irradiated boundary region. However, if the stratified sample is measured in a Raman reflection setup in front of a white diffusely reflecting surface, it is possible to monitor the whole depth of a multiple scattering sample with equal statistical weight. This may be a favorable approach for inline Raman spectroscopy in process analytical technology.

Keywords Reflection and transmission Raman spectroscopy · Diffuse light scattering · Process analytical technology (PAT) · Pharmaceutical analysis · Monte Carlo simulations · Random walk

Introduction

There is an increasing demand for analytical techniques based on Raman radiation generated in the volume of a multiple scattering sample [1, 2]. Areas of application are inline process monitoring [3] with fast-quality control in pharmaceutical manufacturing [4–6], in situ characterization of surface reactions on supported catalysts [7], counterfeit detection of pharmaceutical products through the packaging [8], noninvasive characterization of tissues [9], or bone diseases [10] in medicine and security screenings through bottles, e.g., for the detection of solid and liquid explosives and illicit drugs [11]. Several approaches to quantify active pharmaceutical ingredients in pharmaceutical mixtures by transmission Raman spectroscopy in combination with multivariate data analysis have been published [5, 12, 13]. Applications for the measurement of Raman radiation of diffusely reflecting and transmitting materials have been proposed [14].

Raman radiation originates in the volume of the cited materials mainly from multiple scattered primary radiation, and the Raman signal itself is also elastically scattered many times before it leaves the sample. Hence, the external spatial distribution of Raman radiation depends strongly on the

D. Oelkrug (✉)
Institute of Physical and Theoretical Chemistry,
University of Tübingen, Auf der Morgenstelle 18,
72076 Tübingen, Germany
e-mail: dieter.oelkrug@uni-tuebingen.de

E. Ostertag · R. W. Kessler (✉)
Process Analysis and Technology, Reutlingen Research Institute,
Reutlingen University, Alteburgstr. 150,
72762 Reutlingen, Germany
e-mail: rudolf.kessler@reutlingen-university.de

sample geometry. The simplest situation is met for laterally extended and thick ("semi-infinite") layers with planar boundaries. Here, Raman backscattering is the only applicable measuring geometry. The detected Raman radiation is biased to sample depths close to the irradiated surface ranging from some micrometers to several millimeters, where the depth penetration depends on the albedo and thickness of the sample [15]. Spatially offset Raman spectroscopy [16] marks an approach to overcome the sub-sampling restrictions of conventional backscattering Raman spectroscopy and provides an access to deeper volumes of the sample. Similar to radially resolved diffuse reflectance absorption spectroscopy [17], the detection is separated with a lateral offset to the laser excitation. Raman spectra can be extracted in combination with multivariate data analysis from different depths of turbid samples [16].

In thin samples with typical thicknesses of $z_0 \leq 1$ cm, the backscattering mode can be expanded by forward scattering (= transmission) Raman spectroscopy. This type of detection was worked out already in 1967 by Schrader and Bergmann [18] and received its revival in 2006 by Matousek and Parker [19]. The transmitted Raman signal averages over the whole sample depth with weight maximum in the center of the sample [20, 21]. The weak signal strength of transmitted Raman radiation can be enhanced by a dielectric mirror system [22].

The theoretical analysis of Raman intensities is based almost exclusively on the model of radiative transfer (RT). This model uses geometrical optics and ignores, e.g., interference, diffraction, or polarization of radiation. The most convenient solutions start from the two-flux model of Kubelka–Munk (KM) adding two additional Raman fluxes in the directions of transmission and reflection, respectively. The system of differential equations was first solved for arbitrary layer thicknesses with the approximation that absorption and scattering are independent of the wavelength of radiation [18]. More general solutions can be adapted from the radiation balance of fluorescence in scattering media [23] which behaves formally equal to Raman scattering. Results with wavelength dependent absorption and scattering coefficients were first published for semi-infinite layers [24, 25] and later also for arbitrary layer thicknesses [26–28]. The KM model works well for uniform diffuse irradiation of large sample areas. Laser Raman spectroscopy uses collimated irradiation of small sample areas. Hence, the model has to be modified for these boundary conditions. The full solution of the equation of transfer requires lengthy numerical procedures. However, we have shown that the depth penetration upon normal incidence can excellently be described with the classical diffusion approximation of RT [15], whereas the radial penetration upon spot irradiation requires higher order expansions into spherical harmonics or Monte Carlo simulations [17]. The latter method has already

successfully been applied to describe Raman scattering in turbid media [21].

In this paper, we compare collimated and diffuse irradiation and calculate the transmitted and reflected Raman intensities as function of the layer thickness, absorption coefficient, and scattering coefficient. We emphasize composite layers and describe methods how to enhance the fractions of the desired intensities in forward and backward directions, respectively. The radial spreads of the emitted Raman signals are determined and critically confronted with the limited aperture of the detection system. The calculated results are experimentally tested with organic polymers and basic materials for pharmaceutical tablets. The enhancement of reflected and transmitted Raman intensities by a white diffuse reflectance standard is investigated.

Theory

The termini back- and forward-scattering are well defined for the angular distribution of single scattered radiation. In the multiple scattering regime, there is no principal difference between the angular distributions of radiation from outside sources or inside sources. Both types of radiation become after some scattering processes more or less isotropic and are diffusely reflected or transmitted. In other words, radiation that originally is scattered in forward direction can leave the sample in backward direction, and vice versa. In order to avoid confusion with the single scattering events we use in the following the terminologies "Raman reflection vs. Raman transmission" for the phenomena of emission through the irradiated vs. non-irradiated sample surfaces, and "Raman reflectance vs. Raman transmittance" for the quantitative Raman fluxes leaving the turbid medium. These termini are useful also in cases where one knows nothing about scattering.

Kinetic reaction scheme

A polarizable cylindrical disc of thickness z_0 and radius ρ_0 is irradiated in direction $\cos\theta_0 = \mu_0$ (with θ_0 = angle of incidence) relative to the principal cylinder axis with monochromatic light (Fig. 1). The primary polarizations P move in the sample by multiple elastic scattering processes and leave the disc finally with probability w_R as reflectance R, and with probability w_T as transmittance T. A part of P is absorbed with probability w_A, and part is transformed with probability w_X into Raman excitations X. The latter undergo similar scattering and absorption processes as P.

All partial reaction rates are assumed to be of first order. Table 1 gives definitions of the rate parameters. It is also assumed that Lambert Beer's law is valid for particulate multiple scattering materials, resulting in the attenuation
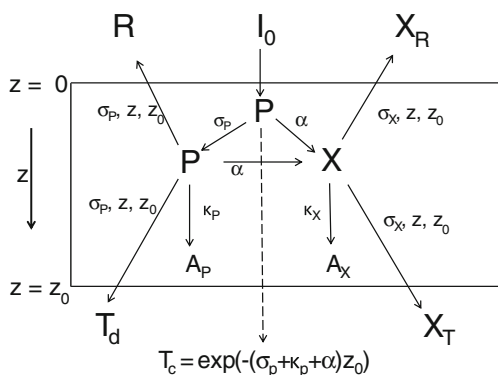
Fig. 1 Kinetic reaction scheme. The primary excitation P moves randomly in the scattering layer of thickness z_0, is diffusely reflected (R), diffusely transmitted (T_d), directly transmitted without being scattered (T_c), absorbed (A_p), or converted into Raman excitation (X). The Raman excitation moves also randomly in the layer, is reflected through the irradiated sample plane (X_R), transmitted through the opposite plane (X_T), or re-absorbed (A_X). Table 1 gives definitions of the rate parameters

approach $\mathrm{dI} = -\mathrm{I}(\sigma + \kappa + \alpha)\mathrm{d}\lambda = -\mathrm{I}\varepsilon\mathrm{d}\lambda$ and the product representations of the differential reaction probabilities

$$\mathrm{dw}_X = \alpha\mathrm{d}\lambda, \mathrm{dw}_A = \kappa_P\mathrm{d}\lambda, \mathrm{dw}'_A = \kappa_X\mathrm{d}\lambda.$$

The formation of Raman excitation is then $\mathrm{d}X = \alpha P\mathrm{d}\lambda$.

The random walk approach

The path length $\Delta\lambda_j$ between scattering event $j-1$ and j is generated as random number $0 < \mathrm{Rnd}_j < 1$ from the probability transformation of Beer's law. The scattering cosine is taken as arbitrary, $\cos\theta = 2\mathrm{Rnd}-1$, (isotropic scattering)

Table 1 Some definitions

λ= length coordinate in arbitrary direction (cm)

λ_R=path length of reflected radiation (cm)

λ_T=path length of transmitted radiation (cm)

α= generation coefficient of Raman radiation (cm^{-1})

κ_P=absorption coefficient of primary radiation (cm^{-1})

κ_X=(re-) absorption coefficient of Raman radiation (cm^{-1})

σ_P, σ_X=elastic scattering coefficient of primary and Raman radiation (cm^{-1})

$\varepsilon = \alpha + \sigma + \kappa$=extinction coefficient (cm^{-1})

μ_0=cosine of angle of incidence θ_0

I_o = intensity of incident light $\left[\frac{\mathrm{W}}{\mathrm{cm}^2}\right]$

z_0=thickness of the sample disc (cm)

ρ_0=radius of the sample disc (cm)

ρ_D=radius of the detected surface area (cm)

$\rho = (x^2 + y^2)^{\frac{1}{2}}$ radial distance from the point of incident primary radiation (cm)

$\Delta\rho$=radial width of a circle ring around the point of incidence (cm)

$$\Delta\lambda_j = -\frac{\ln(\mathrm{Rnd}_j)}{\sigma} \qquad \sum_{\text{entrance}}^{\text{exit}} \Delta\lambda_j = \lambda_R \text{ or } \lambda_T \qquad (1)$$

The total path length from entrance to reflection or transmission, λ_R or λ_T, respectively, is obtained as a sum of path lengths between all scattering events. The layer is irradiated with a large number $N_0 > 10^6$ of very weak light beams ("photons") that can be scattered only in total. The numbers of reflected (N_R) and transmitted (N_T) beams are counted and the individual radial distances (ρ_i) from incidence as well as the individual path lengths ($\lambda_{R,i}$ or $\lambda_{T,i}$) are determined. The reflectance and transmittance of primary light is then

$$R = \frac{1}{N_0}\sum_{i=1}^{N_R} e^{-\kappa_P\lambda_{R,i}} \qquad T = \frac{1}{N_0}\sum_{i=1}^{N_T} e^{-\kappa_P\lambda_{T,i}} \qquad (2)$$

Equations (2) assume attenuation of the beams according to Beer's law under neglect of the very small generation coefficient of Raman excitation ($\alpha < 10^{-7}\,\mathrm{cm}^{-1}$ in dense materials). The corresponding external Raman signals are obtained as solutions of the consecutive first order reaction of scheme 1

$$X_R = \frac{\alpha}{(\kappa_P - \kappa_X)N_0}\sum_{i=1}^{N_R}\left(e^{-\kappa_X\lambda_{R,i}} - e^{-\kappa_P\lambda_{R,i}}\right) \qquad (3a)$$

$$X_T = \frac{\alpha}{(\kappa_P - \kappa_X)N_0}\sum_{i=1}^{N_T}\left(e^{-\kappa_X\lambda_{T,i}} - e^{-\kappa_P\lambda_{T,i}}\right) \qquad (3b)$$

The X signals are made dimensionless (as R and T) by division through the magnitude and dimension unit of the incident primary radiation. Equations (3a) and (3b) assume equal random walk statistics of primary and Raman excitations ($\sigma_P = \sigma_X = \sigma$). The equations simplify for $\kappa_P = \kappa_X = \kappa$ to

$$X_R = \frac{\alpha}{N_0}\sum_{i=1}^{N_R}\lambda_{R,i}e^{-\kappa\lambda_{R,i}} \qquad X_T = \frac{\alpha}{N_0}\sum_{i=1}^{N_T}\lambda_{T,i}e^{-\kappa\lambda_{T,i}} \qquad (4)$$

These relations are reasonable approximations for non-resonant Raman scattering where κ represents some background absorption that does not contribute to the Raman generation coefficient. Finally, the simplest equations are obtained for "quasi-white" multiple scattering materials with negligible absorption, $\kappa \rightarrow 0$

$$X_R = \alpha < \lambda_R > R \qquad X_T = \alpha < \lambda_T > T_d \qquad (5)$$

Where $<\lambda_R>$ and $<\lambda_T>$ are the mean path lengths of reflected and transmitted photons, respectively, and T_d is the scattered transmittance of primary radiation. Equations (5) are acceptable approximations for thick layers. For thin layers, where an important part of the incident radiation is transmitted prior to scattering as $T_c = \exp(-\varepsilon z_0/\mu_0)$, and R and T_d are low, Eqs. (5) must be modified to

$$X_R = \alpha R\left(\frac{1-T_c}{\varepsilon(R+T_d)} + <\lambda_R^* >\right) \quad X_T = \alpha T_d\left(\frac{1-T_c}{\varepsilon(R+T_d)} + >\lambda_T^* >\right) \tag{6}$$

The path lengths λ^* are here counted not from entrance but from the first scattering event. Table 2 presents limiting values for very thin layers with $R \approx T_d \rightarrow 0$, and for very thick nonabsorbing layers with $R \rightarrow 1$.

The analytical approach

Upon homogeneous irradiation, the flux density Φ_P of the primary radiation depends inside the layer only on the depth coordinate z. The Raman flux density is generated according to

$$dX(z) = \alpha \Phi_P(z) dz \tag{7}$$

where Φ_P is normalized to the flux density of the incident irradiation at $z=0$. The integral external Raman intensities emitted as reflectance or transmittance are then [25]

$$X_R = \frac{1}{2}\alpha \int_0^{z_0} \Phi_P(z)\frac{T_{(z)}\left(1+R_{(z_0-z)}\right)}{1-R_{(z)}R_{(z_0-z)}} dz \tag{8a}$$

$$X_T = \frac{1}{2}\alpha \int_0^{z_0} \Phi_P(z)\frac{T_{(z_0-z)}\left(1+R_{(z)}\right)}{1-R_{(z)}R_{(z_0-z)}} dz \tag{8b}$$

Equations (8a and 8b) assumes isotropic angular distribution of Φ_P. The other integrands denote reflectances and transmittances at the Raman wavelength of layers with virtual thicknesses of z and z_0-z, respectively. Analytical solutions of Eqs. (8a and 8b) were obtained for $\sigma_P=\sigma_X$, $\kappa_P=\kappa_X$ and diffuse irradiation [18] using the Kubelka-Munk model as well as for the more general case of arbitrary optical parameters [26–28]. All quantities that are necessary for solving the integrals upon normal incidence can be found in [15]. The

simplest solutions of Eqs. (8a and 8b) are obtainable upon diffuse incidence for white pigments with $\sigma_P=\sigma_X=\sigma$ and $\kappa=0$. The corresponding transmittances and reflectances are inserted from column 5 of Table 2, and the flux density of primary radiation is assumed to decrease linearly with z according to Fick's law (see also Kubelka [29])

$$\Phi_P(z,z_0) = \frac{2(1+2(\tau_0-\tau))}{1+\tau_0} \tag{9}$$

where $\tau=3\sigma z/4$ and $\tau_0=3\sigma z_0/4$. Integration over z_0 yields for nonabsorbing layers

$$X_R = \alpha\left(1+\frac{\tau_0^2}{3(1+\tau_0)^2}\right)z_0 \quad X_T = \alpha\left(1-\frac{\tau_0^2}{3(1+\tau_0)^2}\right)z_0 \tag{10}$$

Limiting values are summarized in Table 2. In the single scattering regime ($\sigma z_0 \ll 1$), the transmittances and reflectances of primary and Raman radiation show the same linear increase with the layer thickness z_0. In the multiple scattering regime ($\sigma z_0 \gg 1$), the reflectance of primary radiation approaches unity and the transmittance decreases hyperbolically with z_0 to zero. In contrast, Raman reflectance and Raman transmittance rise steadily with z_0 approaching for thick layers a constant ratio $X_R/X_T=2$ independent of the scattering coefficient and the geometry of irradiation. The high Raman transmittance is a consequence of the long mean pathway $<\lambda_T>$ of transmitted radiation that rises with z_0^2 and overcompensates the z_0^{-1} decrease of T_d, resulting according to Eq. (5) in a linear increase of X_T with z_0.

Influence of background absorption

Results for weakly absorbing multiple scattering layers

Completely nonabsorbing materials are fiction. The absorption coefficient can be as low as $\kappa=10^{-6}$ cm^{-1}, corresponding to damping of 0.5 dBkm^{-1}, which is typical for optical glass fiber cables in the NIR. In polymeric hydrocarbons the damping at $\lambda=600–1,000$ nm is higher due to the absorption of C–

Table 2 Some properties of nonabsorbing, multiple scattering layers for the limiting cases of very small (columns 2 and 3) and very large optical thicknesses (columns 4 and 5)

Parameter	Low optical thickness $1 \gg \sigma z_0$		High optical thickness $\sigma z_0 \gg 1$	
	Normal incidence	Diffuse incidence	Normal incidence	Diffuse incidence
Scattered transmittance T_d	$\frac{\sigma z_0}{2}$	σz_0	$\frac{5}{4+3\sigma z_0}$	$\frac{4}{4+3\sigma z_0}$
Scattered reflectance R	$\frac{\sigma z_0}{2}$	σz_0	$1 - T_d$	$1 - T_d$
Mean path length $<\lambda_T>$ of scattered transmittance	$\approx 3z_0$	$\approx 5z_0$	$\frac{\sigma z_0^2}{2}$	$\frac{\sigma z_0^2}{2}$
Mean path length $<\lambda_R>$ of scattered reflectance	$\approx 3z_0$	$\approx 5z_0$	$\frac{5z_0}{3}$	$\frac{4z_0}{3}$
RAMAN transmittance X_T	$\alpha\frac{z_0}{2}$	αz_0	$\alpha\frac{5z_0}{6}$	$\alpha\frac{2z_0}{3}$
RAMAN reflectance X_R	$\alpha\frac{z_0}{2}$	αz_0	$\alpha\frac{5z_0}{3}$	$\alpha\frac{4z_0}{3}$

Only the most prominent terms are considered

H vibration overtones, and in functional low molecular materials, the absorption increases further due to forbidden electronic singlet-triplet (π,π^*) or (n,π^*) transitions. In addition, the absorption of fine powders can increase by adsorbed impurities or coordinatively unsaturated surface states. Figure 2 depicts calculated Raman intensities of weak absorbers with diffuse reflectances $R_\infty >$ 0.9. For thin layers, the Raman intensity increases almost linearly with z_0, but then the rise becomes smaller. For thick layers, the reflected intensity X_R saturates at levels that depend strongly on the absorption coefficient. The transmitted intensity X_T passes through a maximum and decreases then exponentially with z_0 to zero. As shown in curves No. 3 of Fig. 2, the model of calculation is of secondary importance. Equations (4) and (8a and 8b) yield equal results in the region of practical interest. Only for very thin layers, $\tau_0 < 3$, the random walk approach produces slightly higher Raman intensities than the diffusion approach. However, these differences cannot be visualized in the scale range of Fig. 2. The strong decrease of X_T with absorption is a consequence of the long path length of transmitted radiation. Especially the long branch of the λ_T distribution is subjected to attenuation resulting in a strong reduction of the mean value $<\lambda_T>$ as well as of the transmittance T_d, and finally to complete damping of Raman transmission in thick layers. Note the different intensity scales for X_R and X_T.

From the practical point of view, it is noteworthy that absorption can be ignored in layers not thicker than 3 mm, which are typical for many pharmaceutical tablets, when the maximum diffuse reflectance exceeds $R_\infty > 0.97$.

Results for thick absorbing multiple scattering layers

The saturation of Raman reflection and the exponential damping of Raman transmission (see curves 3 and 4 in Fig. 2) is calculated from Eqs. (8a and 8b) for the limit of thick absorbing layers and the boundary conditions $\sigma_P = \sigma_X = \sigma$, $\kappa_P = \kappa_X = \kappa$, $\sigma \gg \kappa$

$$\lim_{\gamma z_0 \gg 1} X_R \equiv X_\infty = \frac{2\alpha}{\gamma} R_\infty \qquad (11)$$

$$\lim_{\gamma z_0 \gg 1} X_T = X_\infty (\gamma z_0 - R_\infty) e^{-\gamma z_0} \qquad (12)$$

Here, γ is the attenuation coefficient that can be expressed in the isotropic diffusion approximation or in terms of the Kubelka–Munk scattering (S_{KM}) and absorption (K_{KM}) coefficients as

$$\gamma = 3^{1/2} \left(\kappa^2 + \kappa \sigma \right)^{1/2} \cong b S_{KM} \approx (2 K_{KM} S_{KM})^{1/2} \qquad (13)$$

where $b = (a^2 - 1)^{1/2}$ and $a = (S_{KM} + K_{KM})/S_{KM}$. The diffuse reflectance of optically thick layers is $R_\infty = a - b$.

The reflected Raman signal X_∞ is independent of the layer thickness and proportional to the generation coefficient α, i.e., proportional to the density of the Raman active species. However, the signal is also very sensitive to attenuation by background absorption, as can be seen from Fig. 3. Hence, the analytical application to thick layers makes sense only if the background absorption can be kept as constant. The corresponding transmitted signal $X_{T\infty}$ is very weak and decreases exponentially with the background absorption and the layer thickness. It should be noted that

Fig. 2 Calculated Raman intensities in reflection mode (*left*) and transmission mode (*right*) of multiple scattering layers upon diffuse irradiation inserting a typical scattering coefficient of microcrystalline powders and small absorption coefficients as parameter. See table for details. The smooth lines are calculated with Eqs. (8a and 8b) for $\kappa_p = \kappa_x = \kappa$; the noisy lines are simulated with the random walk model of Eqs. (1) and (4). The two calculation methods yield indistinguishable results. Note the different ordinate scales of the two graphs
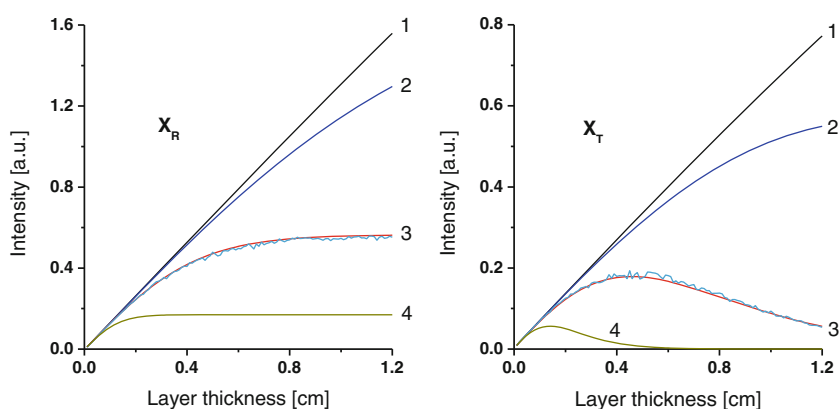
Scattering coefficient: $\sigma = 200$ cm^{-1}				
Curve	Absorption coefficient κ [cm^{-1}]	Albedo $\omega = \sigma(\sigma+\kappa)^{-1}$	Diffuse Reflectance R_∞ (for $z_0 \rightarrow \infty$)	Attenuation coefficient γ [cm^{-1}], see eq. (13)
1	0.0002	0.999999	0.998	0.35
2	0.002	0.99999	0.993	1.10
3	0.02	0.9999	0.977	3.46
4	0.2	0.999	0.930	10.96

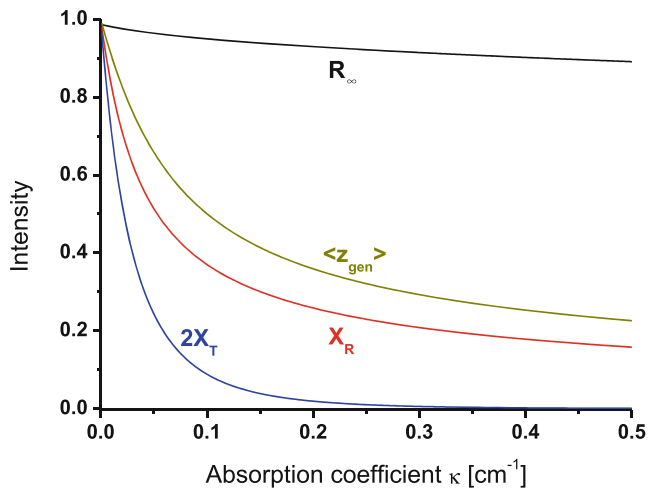**Fig. 3** Raman intensities X_R and X_T, diffuse reflectance R, mean generation depth $<z_{gen}>$ of X_R of an optically thick scattering layer with $\sigma=200$ cm^{-1}, $z_0=0.5$ cm as function of the background absorption coefficient κ. The reflectance is presented in absolute values. Other data are normalized to unity at $\kappa=0$, where $<z_{gen}>=0.124$ cm

both types of Raman signals decrease much stronger with the absorption coefficient than the diffuse reflectance of primary radiation.

Axial generation depth profiles of Raman signals in multiple scattering, nonabsorbing layers

The differentials of Eqs. (8a and 8b) directly yield the depth profiles of Raman generation emitted as X_R and X_T, respectively. Alternatively, the profiles are available from the random walk approach [21]. Figure 4 presents the result of
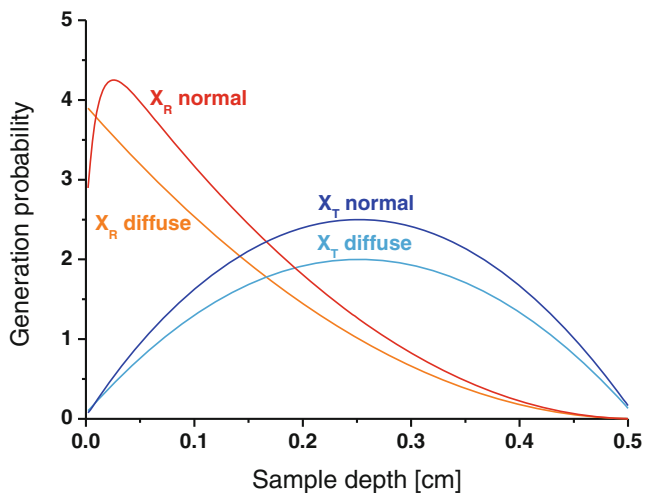

Fig. 4 Depth origins of Raman emission in a scattering layer ($z_0=$ 0.5 cm, $\sigma=100$ cm^{-1}, and $\kappa=0$). X_R emission in the reflection mode, X_T emission in the transmission mode. Comparison of diffuse irradiation and collimated irradiation of normal incidence ($\mu_0=1$). Note: X_T is magnified against X_R by a factor of 2

the diffusion approximation for a nonabsorbing layer. The reflected Raman signal originates mainly from regions facing the irradiated surface. Upon diffuse incidence, the contributions to X_R is proportional to $(\Phi_p(z))^2$ and falls off monotonically with z. The mean value of the generation depth approaches $<z_{XR}>\approx0.25\ z_0$, almost independent of the scattering coefficient and its anisotropy. Upon normal incidence, the generation profile of X_R passes through a maximum close to the irradiated surface. Then the profile decays in a similar way as for diffuse irradiation. The transmitted Raman signal is generated mainly in the deep interior of the layer. The generation profile follows approximately a symmetric parabola with the apex in the center of the layer. Hence, X_T probes mainly the central regions whereas the boundaries contribute only little to the signal.

Radial spread of Raman intensities in multiple scattering, nonabsorbing layers

The distance between photon incidence and photon emission is an important parameter, e.g., the design of detection units or for the resolution of spectral images. The general analytical solution of the trinomial system (σ, κ, and z_0) is not yet available. We prefer the numerical random-walk approach and determine the number of reflected, $N_R(\rho)$, and transmitted, $N_T(\rho)$, photons as function of the distance ρ from the axis of incidence, as well as the associated path lengths $\lambda_R(\rho)$ and $\lambda_T(\rho)$. From these quantities and Eqs. (5) or (6), the radial Raman intensities are accessible. The result for nonabsorbing layers with negligible contribution of collimated transmittance T_c is then

$$\frac{\Delta X_R}{\Delta \rho} \equiv X_R'(\rho) = \alpha R'(\rho)\left(\sigma^{-1}+ < \lambda_R^*(\rho) >\right)$$
$$\frac{\Delta X_T}{\Delta \rho} \equiv X_T'(\rho) = \alpha T_d'(\rho)\ \left(\sigma^{-1}+ < \lambda_T^*(\rho) >\right)$$
(14)

where R' and T_d' are the distant dependent radial reflectances and transmittances of the primary radiation, respectively, per circle ring of width $\Delta\rho$. The radial spreads of $R'(\rho)$ and $T'(\rho)$ upon point irradiation are extensively described in [30]. In order to simplify the evaluation of Eq. (14), the scattering coefficient is assumed to be independent of the wavelength. Further assumptions are $\sigma>>>\alpha$ and $\sigma>>z_0^{-1}$.

Figure 5 summarizes representative radial intensity distributions of reflected and transmitted Raman signals. Neglecting secondary terms, the main features are as follows:

The radial width of the transmitted signal X_T' is linearly proportional to the layer thickness z_0 and almost independent of the scattering coefficient σ. The amplitude of X_T' is independent of z_0 and σ. The mean radial spread can be approximated by

$$< \rho_{X_T} >= \sigma^{-1} + (2/3)^{1/2}z_0$$
(15)

Fig. 5 Numerical random-walk approach: calculated radial Raman intensities in reflectance and transmittance directions as function of the radial distance ρ from the axis of incidence ($\mu_0=1$). Number of incident photons $N_0=1E^7$. *Left part*, $z_0=0.1$ cm, $\sigma=100$ cm^{-1}. *Right part*, $z_0=0.2$ cm, $\sigma=50$, and 100 cm^{-1}. Radial resolution $\Delta\rho=0.001$ cm (*left curves*) and, in order to reduce noise, $\Delta\rho=0.01$ cm (*right curves*). Note the equal ordinate but different abscissa scales
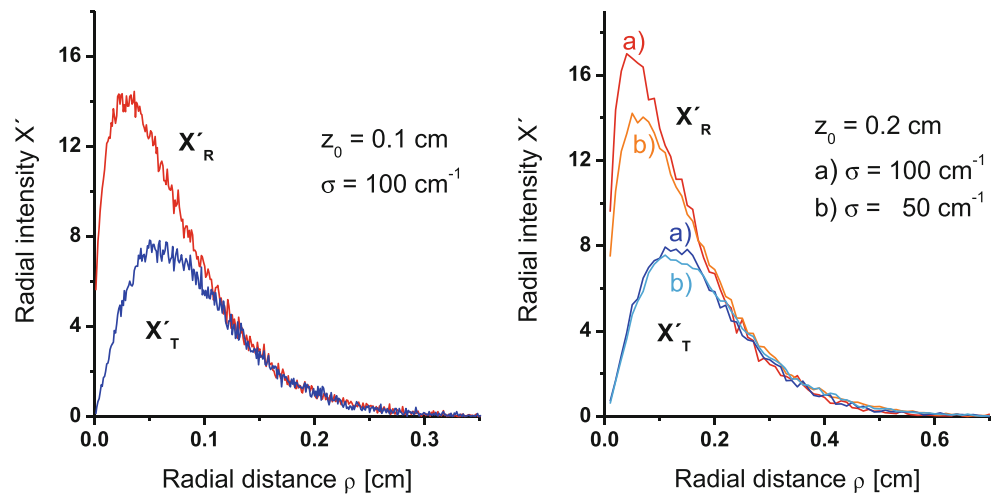
However, the long distance tail extends much wider than the mean value. Hence, the sample radius should be $\rho_0 \geq 3z_0$ in order to obtain quantitative correct transmission intensities. Ignoring the small contribution of the scattering coefficient, the binomial radial distribution of X_T' can be approximated in the nonabsorbing multi-scattering limit by a Gaussian distribution with a pre-exponential factor that normalizes the ($0 \leq \rho \leq \infty$)—integral of the square bracket to unity.

$$X_T' = \left[\frac{\sqrt{3\pi}\ \rho}{(z_0)^2} \ \exp\left(-\frac{2}{3} \frac{\left(\frac{z_0}{2}+\rho\right)^2}{(z_0)^2} \right) \right] X_T \qquad (16)$$

Despite its approximate character, Eq. (16) reproduces the radial spread of X_T over a wide range of layer thicknesses and scattering coefficients. Figure 6 shows the radial spread of Raman transmittance X_T' from multiple scattering layers for layer thicknesses from 0.1 to 0.5 cm based on the analytical approximation of Eq. (16) and on Monte-Carlo simulations. The analytical approximation matches closely
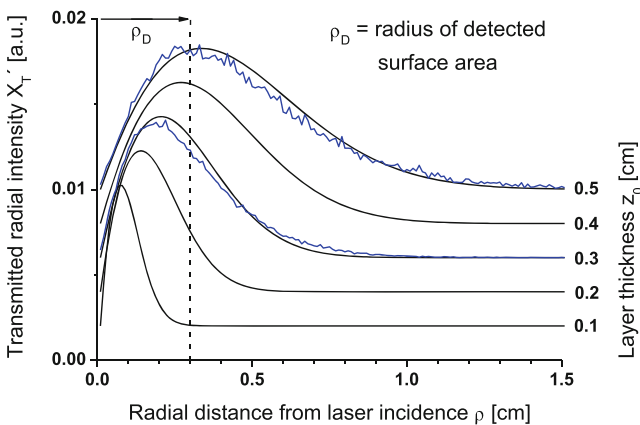
the Monte-Carlo simulations. Figure 6 demonstrates clearly that quantitative intensity conclusions in a transmission setup should only be drawn for layer thicknesses not substantially greater than 0.1 cm if the radius ρ_D of the detected surface area is limited to 0.3 cm.

The radial distribution of Raman reflectance behaves more complex than Eq. (16), and we did not yet find a satisfying analytical approximation. The X_R'—range of very small distances $\rho < \sigma^{-1}$ depends predominantly on the scattering coefficient. The range $\sigma^{-1} < \rho < z_0$ of medium distances depends both on the scattering coefficient and on the layer thickness. The far-distance range $\rho > z_0$ becomes equal to X_T', see Fig. 5. Here, the density Φ_P of primary radiation is distributed symmetrically to the central layer plane ($z=z_0/2$) resulting in equal probabilities for reflectance and transmittance. Despite its complex nature, the mean value of radial spread yields in good approximation

$$< \rho_{X_R} > \approx 0.5 z_0 \qquad (17)$$

However, this equation does not render the wide spread of the long distance tail that requires sample radii and detector apertures as large as in the transmission mode in order to acquire correct reflectance intensities.

Experimental

The Raman reflection and transmission spectra are measured with the nonconfocal RamanRXN1™ analyzer from Kaiser Optical Systems, Ann Arbor, MI equipped with an Invictus™ 785-nm NIR diode laser specified for a maximum output power of 450 mW. The laser irradiates the sample via an optical fiber and additional optics with an accessible wavelength range of $\Delta\nu=0$ to 1,800 cm^{-1} Raman shift.

Figure 7 presents schematically the irradiation and detection geometries of the analyzer. The Raman radiation is

Fig. 6 Radial spread of Raman transmittance X_T' from multiple scattering layers of different thicknesses. *Smooth lines*, analytical approximation; *noisy lines*, two examples of Monte-Carlo simulations. ρ_D radius of detected surface area. Curves are vertically displaced
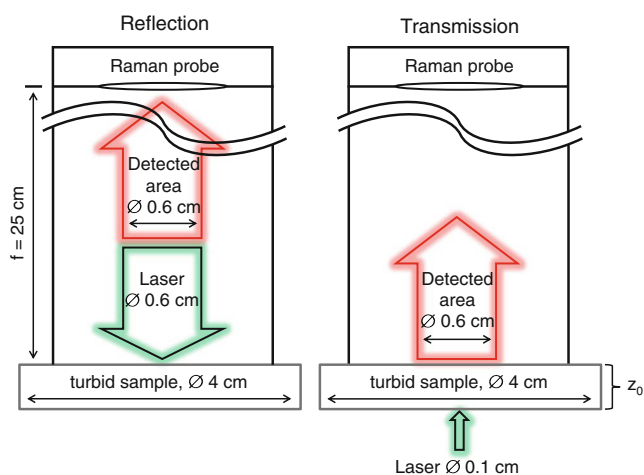
Fig. 7 Raman measurements on a cylindrical sample with variable thickness z_0 and fixed diameter $2\rho_0$=4 cm in the setups for reflection (*left*) and transmission (*right*).The Raman radiation is collected in both cases with the PhAT™ head. A circular area of the sample with 0.6 cm diameter is imaged via a lens with 25-cm focal length onto the Raman probe. In the reflection setup, a laser illuminates the sample via an optical fiber and the focusing lens from top with a circular area of 0.6 cm diameter. In the transmission setup, a laser illuminates the bottom side of the sample with 0.1 mm beam diameter

collected in both the reflection and transmission setup via an array of 50 optical fibers (PhAT™ probe). In the reflection setup a circular area of the sample is homogeneously irradiated via one optical fiber and f=25 cm optics. The irradiated area with diameter of 0.6 cm is much smaller than the total sample area. The emitted Raman radiation and reflected primary radiation are collected via the PhAT™ probe, carefully separated with filter elements and then transferred to the volume phase transmission grating and the Peltier cooled CCD matrix detector to generate the Raman spectra. In the transmission setup, the laser is guided into a transmission illuminator that irradiates the bottom side of the sample with a diameter of 0.1 cm. The detection unit is the same as for the reflection setup. The Raman intensities X_R and X_T in reflection and transmission are calibrated with liquid cyclohexane in a thin optical cuvette.

A Lambda 9™ spectrophotometer from PerkinElmer, Waltham, MA with integrating sphere is used for determining the scattering coefficient of poly-tetrafluorethylene (PTFE, Teflon™) by measuring in diffuse transmission and diffuse reflection spectra followed by calculations with the diffusion model [15].

PTFE as optical diffuse material for thickness dependent investigations is supplied by GigahertzOptik, Türkenfeld, Germany in thicknesses of 0.02 and 0.15 cm. Additional thicknesses up to 0.5 cm were cut from a PTFE cylinder with 4 cm diameter or prepared as stacks from the 0.02 cm layer. Cellulose is purchased as filters type MN 615 from Macherey-Nagel, Düren, Germany with 0.015 cm thickness. Acetylsalicylic acid (ASA), product No. 158185000 from

Acros Organics, Geel, Belgium, is used to press a cylindrical disc with 2 cm diameter and 0.425 cm thickness as inner layer of a composite triple layer. The upper and the lower layer consists of a PTFE layer (Fig. 11). A white diffuse reflectance standard is produced with a powder press using $BaSO_4$, product No. 11845 from FlukaChemie, Buchs, Switzerland. Thin layers of PTFE and cellulose are placed on the white standard in reflection setup to demonstrate a Raman enhancement (Fig. 13).

Experimental results and discussion

Raman intensity as function of the layer thickness

The calculated Raman intensities in transmission and reflection modes are experimentally tested with PTFE layers of different thicknesses z_0=0.02–0.5 cm. The material is strongly scattering, quasi nonabsorbing in the vis–NIR range, and its Raman spectrum is well known [14, 31–33]. We evaluate especially the emission at v=733 cm^{-1} Raman shift (A_1 stretching mode $v_s(CF_2)$) which marks the most intense band in the PTFE Raman spectrum, and the intense sub-band of the characteristic PTFE-triplet located at v= 1,382 cm^{-1} Raman shift (a component of two split F_2 symmetry lines [34, 35], exact assignment not yet available).

Figure 8 summarizes the experimental results. Up to $z_0 \leq$ 0.15 cm, the measured intensities increase linearly with the layer thickness. Then X_R flattens, and X_T passes through a maximum. We determine the scattering coefficient of PTFE from the diffuse reflectance and transmittance of a thin layer to σ_{800}=220 cm^{-1} and then fit the Raman data with the help of Eqs. (8a and 8b). Both X_R and X_T can be reproduced with the same apparent absorption coefficient of κ_{app}=0.029 cm^{-1} (see the curved lines in Fig. 8), corresponding to an albedo of ω=0.99986 and a maximum diffuse reflectance of R_∞= 0.975. This range of data sets is often found in the literature for "white" pigment powders. However, if one looks critically on PTFE as highly pure material with negligible vibrational overtone or electronic absorption, the experimental absorption coefficient seems to be extremely high. Hence, we include the constant detector aperture and the strongly z_0-dependent radial Raman spread in the evaluation process (for illustration, see Fig. 6, where it becomes obvious that not all transmitted radiation is collected for thick layers with our detection system, thus quantitative intensity conclusions require aperture radii greater than three times the layer thicknesses), and obtain linear intensity correlations up to z_0= 0.5 cm for the reflected as well as for the transmitted Raman radiation. The correction reduces the absorption coefficient to a reasonable value of $\kappa < 10^{-3}$ cm^{-1} and increases the maximum diffuse reflectance to $R_\infty > 0.995$. It should be noticed
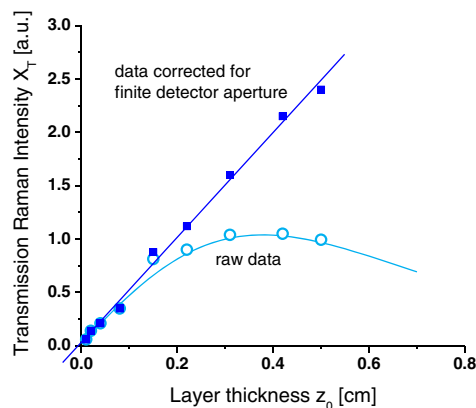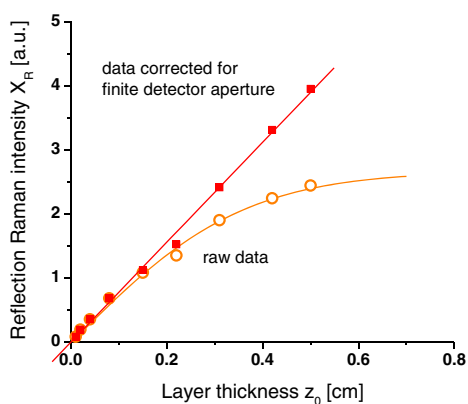
Fig. 8 Reflection and transmission Raman intensities at $\Delta\nu=$ 1,382 cm^{-1} Raman shift (X_R, *left* and X_T, *right*) as function of the thickness of PTFE layers. The open circles represent the raw data from the experiment. The curved lines are calculated for X_R and X_T with the same absorption coefficient $\kappa=0.029$ cm^{-1} and $\sigma=200$ cm^{-1}. The *solid squares with fitted straight lines* show the Raman data corrected for finite detector aperture with the help of radial intensity spread curves as in Figs. 5 and 6

that detection losses due to the wide radial spread of transmitted signals is one of the main error sources for quantitative determination of small absorption coefficients in scattering materials.

Composite layers

Double layers

Double layers with two axially separated different Raman emitters A and B produce signals that do not depend only on the thickness of the emitting layer but also on the thickness and position of the co-layer. Figure 9 illustrates the situation for given emitter thickness and variable co-layer thickness.
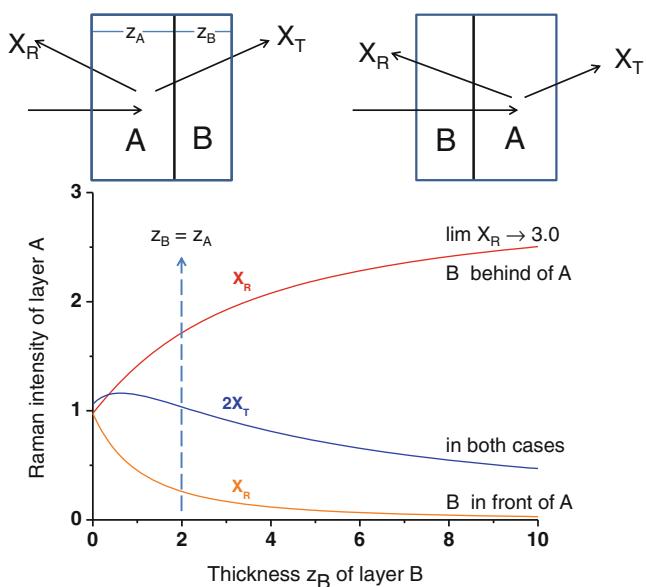

Fig. 9 Reflected and transmitted Raman intensities of a scattering layer A of thickness $z_A=0.2$ cm in contact with a second layer B of variable thickness z_B. Diffuse irradiation. X_R is normalized to unity for $z_B=0$. ($\sigma=100$ cm^{-1}, $\kappa=0$, for both layers)

The reflected Raman intensity X_R of the front layer increases strongly with the thickness of the back layer because part of the initially transmitted Raman signal is now reflected, but mainly because the density Φ_P of the primary radiation becomes higher. The reflected intensity of the back layer behaves in the opposite way. If we assume equal thicknesses, $z_A=z_B=z_0/2$, then the reflected signal is determined to about 85 % by the front layer and only to 15 % by the back layer. The experimental result is shown in Fig. 13. The ratio in this example is 80 and 20 %, here it has to be taken into account, that the layers do not possess equal thicknesses.

The experiment in reflection geometry (Fig. 10, graphs X_R) proves this result in acceptable accuracy. The double layer of cellulose and PTFE is irradiated alternatively from one of the two sides. The PTFE signal from the front side is approximately four times as high as from the back side (see, e.g., the Raman band of PTFE at 1,382 cm^{-1}).

Contrary to X_R, transmission Raman spectra are expected to be independent of the side of irradiation, see Fig. 9. In both arrangements, X_T first increases with the co-layer thickness and then falls down slowly to zero. The spectra of Fig. 10 prove experimentally the independency of the side of irradiation in transmission geometry with a double layer of PTFE and cellulose.

Triple layers

Triple layers $A/B/A$ simulate coated or encapsulated powders, and are expected according to Fig. 4 to behave as follows: X_R highlights the spectrum of A, X_T highlights the spectrum of B since the generation probability of the central layer is much higher than of the border layers.

Figure 11 shows experimental data for a triple layer arrangement of PTFE (0.15 cm)/ASA (0.425 cm)/PTFE (0.15 cm). The Raman band at 733 cm^{-1} shift originates
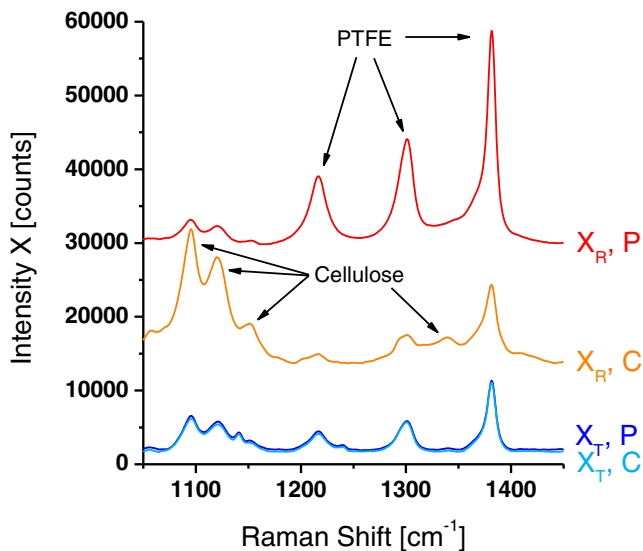
Fig. 10 Raman reflection and transmission intensities X_R and X_T of a double layer of 0.020 cm PTFE and 0.015 cm cellulose with *P* orientation of PTFE to the detector and *C* orientation of cellulose to the detector. The spectra are fluorescence corrected. The reflection spectra differ clearly from each other; the transmission spectra coincide nearly perfectly and show the independence from the side of irradiation. The reflection spectra are vertically displaced to the transmission spectra

from PTFE, the three other bands from ASA. The Raman reflection setup emphasizes clearly the spectrum of PTFE, the transmission setup the spectrum of ASA.

Stack of layers

Stack of layers allow to assign the position of a given component in a multi-layer of a second component. We
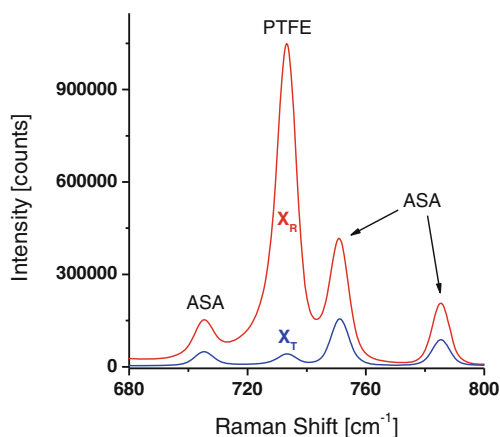
investigate the Raman emission of an ASA layer in a stack of four additional mannitol layers as function of the position of ASA. The central position yields much more intense X_T-spectra than the border position. Figure 12 compares the experimental data of Svensson et al. (presented at FACSS 2009 [30]) with model calculations according to Fig. 3. The correlation is not perfect but it shows clearly that the central layer regions contribute more to the transmission Raman signal than the border layers.

Enhancement of reflected or transmitted Raman intensities by a white diffuse reflectance standard

Reflecting optical elements are widely used for luminance or contrast amplification. Matousek [22] described an elegant method of Raman enhancement with the help of dielectric mirrors and band-pass filters. In this chapter, we substitute the mirrors by diffuse reflectance standards which are suitable for on-line applications and easy to use over a wide wavelength range. For reflectance enhancement, the thin Raman active layer with diffuse reflectance R_0 and transmittance T_0 is placed in front of a thick standard like microcrystalline barium sulfate ($BaSO_4$) or elemental sulfur, and irradiated with intensity $I_0 = 1$. For random walk simulations and analytical solutions with the diffusion approximation we use normal incidence which comes close to the experimental condition of Raman excitation. For demonstration of the principal effects we simplify to diffuse incidence. The transmitted light T_0 is repeatedly reflected between the standard and the layer resulting in back-irradiation of the layer with intensity

$$J_B = \frac{T_0 R_B}{1 - R_0 R_B} \tag{18}$$

Fig. 11 Raman reflection (X_R) and transmission intensities (X_T) from a composite triple layer system of PTFE 0.15 cm/ASA 0.425 cm/PTFE 0.15 cm. The band at 733 cm^{-1} Raman shift results from PTFE and is assigned to $\nu_s(CF_2)$Sym. A1. The remaining bands are assigned to acetylsalicylic acid. The Raman spectrum of ASA does not comprise a band at $\Delta\nu = 733$ cm^{-1}
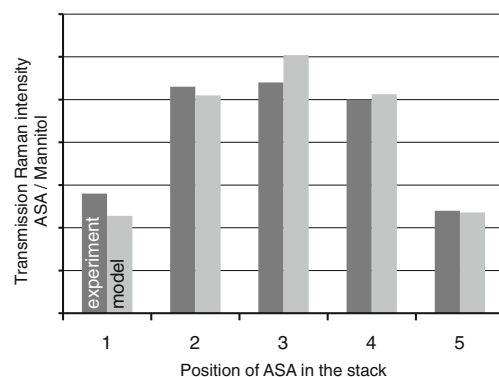

Fig. 12 Transmitted Raman intensity X_T (ASA/Mannitol) of a 0.1-cm ASA layer in a stack of four additional 0.1 cm mannitol layers as function of the position of ASA in the stack. The experimental results are compared with model calculations according to Fig. 3. Intensities are relative to the sum of all five positions. Experimental results were presented by Svensson et al. at FACSS 2009 [30]

where R_B is the diffuse reflectance of the standard. We neglect absorption, which is a reasonable approximation in thin "white" layers, resulting in $R_0 + T_0 = 1$, and assume a perfect reflectance standard with $R_B = 1$. Then Eq. (18) simplifies to

$$J_B = 1 = I_0 \qquad (19)$$

The layer is irradiated in this case from both sides with the same intensity. As consequence, the density of the exciting radiation which decays in the free-standing layer linearly with the sample depth, see Eq. (9), is now doubled with its mirror image $\Phi_{p,\,backward}$ resulting in a constant density over the whole layer thickness

$$\Phi_{p,\,tot} = \Phi_{p,\,forward} + \Phi_{p,\,backward} = 4 \qquad (20)$$

Upon normal incidence $\mu_0 = 1$, the transmittance and thus the back-radiation density at τ_0 increases against diffuse incidence by a factor of 5/4 (see Table 2), and the density at $\tau = 0$ starts with a lower value of three

$$\Phi_{p,\,tot(\mu 0=1)} \approx 5 - 2\exp(-2\tau) \qquad (21)$$

The expected enhancement of Raman reflectance is then a product of two factors

1. The transmitted part X_T is backscattered and enhances X_R by a factor of 1.5 (thick layers) up to a factor of 2 (very thin layers), see Table 2;
2. The density of primary radiation increases upon diffuse incidence by a factor of 2, and upon normal incidence by a factor of ≤ 2.5.

Hence, the total enhancement lies somewhere between a factor of _3_ and _4_.

Figure 13 presents a series of experimental results on a thin PTFE layer (0.02 ± 0.001 cm) in combination with a thin cellulose layer (0.015 ± 0.002 cm) and a thick BaSO$_4$ reflectance standard (0.5 cm). The Raman intensities are normalized to the backscattered band maximum X_R at $\Delta\nu = 733$ cm^{-1} of the single PTFE layer.

Addition of the cellulose layer as background strongly increases X_R of PTFE (case II of Fig. 13) whereas X_T remains almost unaffected. Addition of cellulose as foreground (case III) strongly reduces X_R whereas X_T remains again almost unaffected. These results are often quoted as argument that X_T is superior to X_R in composite systems since X_R probes only the regions close to the surface whereas X_T probes also the deep parts of the sample. The cases V and VI of Fig. 13 give clear evidence how to overcome these restrictions. The bi-layer system is now measured in both orientations on the BaSO$_4$ standard. The backscattered intensity increases _in both orientations_ strongly against the free-standing bi-layer. The increase of case VI with PTFE inside is even somewhat stronger than case V with PTFE directly exposed to the laser. Most of the results agree with the model calculations of Fig. 9 and Eqs. (18)–(20) for diffuse incidence. The increase from case V to case VI can be explained only with normal incidence where, according to Eq. (21), the deep layer produces somewhat higher signals than the layer directly exposed to the surface. Apart from these minor corrections, the general statement is valid for analytical applications: Raman reflection spectroscopy probes the whole depth of a multiple scattering sample with equal statistical weight if the sample is placed in front of a white diffuse reflector.

Figure 14 illustrates case IV of Fig. 13 with three prominent Raman bands of a thin PTFE layer placed on a BaSO$_4$ diffuse reflectance standard. The Raman reflection signals are intensified approximately by a factor of 3.5 relative to the self-supporting PTFE layer of case I.

Enhancement of X_T can be achieved with a white diffuse reflector in front of the Ramanactive layer. The front reflector contains a small pinhole of diameter $d \leq$ 1 mm for collimated laser irradiation. The pinhole reduces the effective diffuse reflectance of the front reflector to $R_{eff} < 1$, where the reduction depends on the radial spreads of the reflected primary and Raman radiations. The repeated reflection of I_0 between the Raman
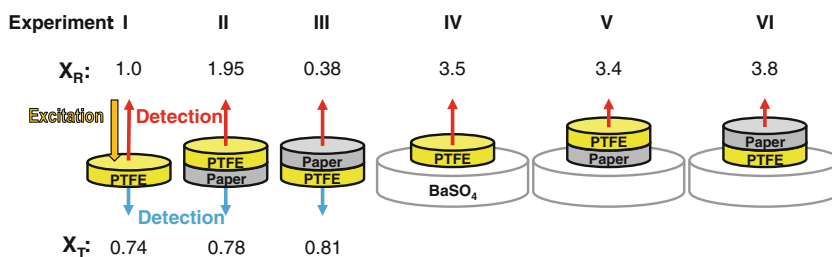

Fig. 13 Experimental Raman intensities (integrated emission band with maximum at $\Delta\nu = 733$ cm^{-1}) of PTFE with layer thickness $z_0 = 0.02$ cm in different configurations. _I_, Free-standing layer; _II_, in front of a cellulose filter paper with thickness $z_0 = 0.015$ cm; _III_, behind the paper, _IV_: PTFE on a thick BaSO$_4$ diffuse reflectance standard; _V_, configuration II on BaSO$_4$; _VI_, configuration III on BaSO$_4$. The remitted Raman intensity of the single PTFE-layer is normalized to $X_R = 1$. The experimental errors are $\Delta X \approx \pm 0.02X$
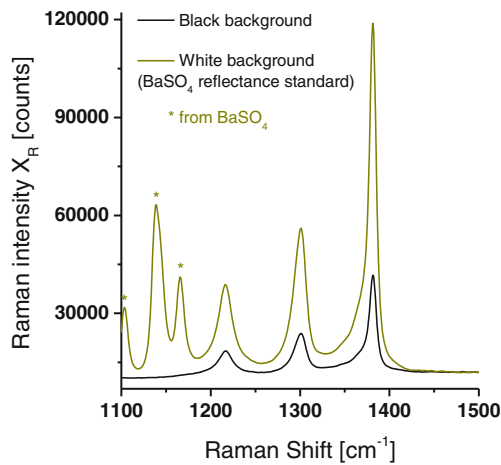
Fig. 14 Detail of Raman reflection spectra of PTFE with layer thickness $z_0 = 0.20$ cm. *Black spectrum*, PTFE self-supporting; *dark yellow spectrum*, PTFE on BaSO$_4$ background (Raman bands with asterisks result from BaSO$_4$). The Raman reflection intensities of the bands at 1,216, 1,301, and 1,382 cm^{-1} of PTFE on BaSO$_4$ are intensified approximately by a factor of 3.5 relative to the self-supporting PTFE layer (intensities from integrated emission bands)

active layer and the front reflector with $R_{p,\ eff}$ produces, similar to Eq. (18), an additional irradiance in forward direction

$$I_F = \frac{R_0 R_{p,\ eff}}{1 - R_0 R_{p,eff}} \qquad (22)$$

The total irradiance is then

$$I_{tot} = I_0 + I_F = \frac{1}{1 - R_0 R_{p,\ eff}} \qquad (23)$$

and, instead of Eq. (9), the radiation density inside the layer is

$$\Phi_{p,\ tot} = \frac{2(1 + 2(\tau_0 - \tau))}{(1 - R_0 R_{p,\ eff})(1 + \tau_0)} \qquad (24)$$

Equation (24) is inserted in Eq. (8b), and the enhanced X_T can be calculated after replacing the reflectance $R_{(z)}$ of the virtual layer without front reflector by the modified reflectance $R_{(z),\ eff}$, that considers the influence of the front reflector with the effective reflectance $R_{X,\ eff}$ for Raman radiation

$$R_{(z),\ eff} = R_{(z)} + \frac{T_{(z)}^2 R_{X,\ eff}}{1 - R_{(z)} R_{X,\ eff}} \qquad (25)$$

The achievable enhancement of X_T depends strongly on the layer thickness and the pinhole diameter. Thin layers as PTFE of Fig. 13 with $z_0 = 0.02$ cm require according to random walk simulations very small pinholes of $d \approx 100$ μm in order to obtain an enhancement by a factor of *five*. The same enhancement is obtained

for thicker layers of $z_0 \approx 0.2$ cm already with a large pinhole of $d \approx 1$ mm.

It should be noted that the signal of highly enhanced X_T is generated mainly close to the irradiated surface and no longer symmetrically to the sample center, as it is the case shown in Fig. 3. Enhanced X_T has lost its ability of deep sample probing and has transferred this quality to enhanced X_R.

Conclusions

In scattering layers with negligible background absorption and no axial concentration gradients, the reflected and transmitted Raman intensities (X_R and X_T) show a linear increase with the layer thickness whereas X_T is at least half as intense as X_R. Under the initially mentioned conditions both the reflection and transmission setups are equally suitable modes. The radial expansion of the signals increases linearly with the layer thickness, where X_T spreads wider than X_R. For correct intensity measurements, the diameter of the detected surface area must be in the transmission mode at least six times the layer thickness.

In scattering layers with some background absorption, the Raman intensities are reduced by re-absorption. X_R saturates for thick layers at levels that depend strongly on the absorption coefficient. X_T passes through a maximum and then reduces to zero. Hence, the R-mode is superior in those cases to the T-mode. The strong decrease of X_T with absorption is a consequence of the long path length of transmitted radiation. Both X_T and X_R decrease much stronger with the absorption coefficient than the diffuse reflectance of primary radiation.

In composite layers with axial concentration gradients we get complementary information from the R- and T-modes. The mean reflected signal originates from the first quarter of the layer depth, whereas the mean transmitted signal originates predominantly from the central regions. Here, for probing the inner volume of a sample the T-mode is superior to the R-mode.

The intensity of Raman signals can be significantly enhanced by reflecting mirrors arranged in the close environment of the sample. We propose especially white diffuse reflectors at the sample backside. This arrangement intensifies X_R by a factor of 3 to 4 and produces constant irradiation densities over the whole sample depth. Hence, X_R probes in this configuration the whole sample with equal statistical weight. Highly enhanced X_T is generated close to the irradiated surface. Enhanced X_T has lost its ability of deep sample probing and has transferred this quality to enhanced X_R. The authors consider enhanced Raman reflection spectroscopy as promising tool for process analytical technology.

References

1. Salzer R, Siesler HW (eds) (2009) Infrared and Raman spectroscopic imaging, 1st edn. Wiley, Weinheim

2. Buckley K, Matousek P (2011) Recent advances in the application of transmission Raman spectroscopy to pharmaceutical analysis. J Pharm Biomed Anal 55:645–652. doi:10.1016/j.jpba.2010.10.029

3. Wikström H, Lewis IR, Taylor LS (2005) Comparison of sampling techniques for in-line monitoring using Raman spectroscopy. Appl Spectrosc 59(7):934–941

4. Kalantri PP, Somani RR, Makhija DT (2010) Raman spectroscopy: a potential technique in analysis of pharmaceuticals. Der Chemica Sinica 1:1–12

5. Johansson J, Sparen A, Svensson O, Folestad S, Claybourn M (2007) Quantitative transmission Raman spectroscopy of pharmaceutical tablets and capsules. Appl Spectrosc 61:1211–1218. doi:10.1366/000370207782597085

6. Sparén A, Johansson J, Svensson O, Folestad S, Clayborn M (2009) Transmission Raman spectroscopy for quantitative analysis of pharmaceutical solids. Am Pharmaceut Rev 62–71

7. Gao X, Jehng J-M, Wachs IE (2002) In situ UV–vis–NIR diffuse reflectance and Raman spectroscopic studies of propane oxidation over ZrO_2-supported vanadium oxide catalysts. J Catal 209(1):43–50. doi:10.1006/jcat.2002.3635

8. Eliasson C, Matousek P (2007) Noninvasive authentication of pharmaceutical products through packaging using spatially offset Raman spectroscopy. Anal Chem 79(4):1696–1701. doi:10.1021/ac062223z

9. Stone N, Baker R, Prieto CH, Matousek P (2008) Novel Raman signal recovery from deeply buried tissue components. In: Mahadevan-Jansen A, Petrich W, Alfano RR, Katz A (eds) Biomedical optical spectroscopy. Proceedings of SPIE. SPIE-OSA, p 68530N. doi:10.1117/12.786442

10. Srinivasan S, Schulmerich M, Cole JH, Dooley KA, Kreider JM, Pogue BW, Morris MD, Goldstein SA (2008) Image-guided Raman spectroscopic recovery of canine cortical bone contrast in situ. Opt Express 16(16):12190–12200

11. Matousek P (2006) Inverse spatially offset Raman spectroscopy for deep noninvasive probing of turbid media. Appl Spectrosc 60(11):1341–1347

12. Eliasson C, Macleod NA, Jayes LC, Clarke FC, Hammond SV, Smith MR, Matousek P (2008) Non-invasive quantitative assessment of the content of pharmaceutical capsules using transmission Raman spectroscopy. J Pharm Biomed Anal 47:221–229. doi:10.1016/j.jpba.2008.01.013

13. Hargreaves MD, MacLeod NA, Smith MR, Andrews D, Hammond SV, Matousek P (2011) Characterization of transmission Raman spectroscopy for rapid quantitative analysis of intact multicomponent pharmaceutical capsules. J Pharm Biomed Anal 54:463–468. doi:10.1016/j.jpba.2010.09.015

14. Nah S, Kim D, Chung H, Han S-H, Yoon M-Y (2007) A new quantitative Raman measurement scheme using Teflon as a novel intensity correction standard as well as the sample container. J Raman Spectros 38(5):475–482. doi:10.1002/jrs.1667

15. Oelkrug D, Brun M, Rebner K, Boldrini B, Kessler RW (2012) Penetration of light into multiple scattering media; model calculations and reflectance experiments. Part I: the axial transfer. Appl Spectrosc 66(8):934–943. doi:10.1366/11-06518

16. Matousek P, Clark IP, Draper ERC, Morris MD, Goodship AE, Everall N, Towrie M, Finney WF, Parker AW (2005) Subsurface probing in diffusely scattering media using spatially offset Raman spectroscopy. Appl Spectrosc 59(4):393–400

17. Oelkrug D, Brun M, Hubner P, Egelhaaf H-J (1996) Optical parameters of turbid materials and tissues as determined by laterally resolved reflectance measurements. Proc SPIE 2925:106–115. doi:10.1117/12.260831

18. Schrader B, Bergmann G (1967) Die Intensität des Ramanspektrums polykristalliner Substanzen. Fresenius J Anal Chem 225(2):230–247. doi:10.1007/bf00983673

19. Matousek P, Parker AW (2006) Bulk Raman analysis of pharmaceutical tablets. Appl Spectrosc 60(12):1353–1357. doi:10.1366/000370206779321463

20. Everall N, Matousek P, MacLeod N, Ronayne KL, Clark IP (2010) Temporal and spatial resolution in transmission Raman spectroscopy. Appl Spectrosc 64:52–60. doi:10.1366/000370210790571963

21. Everall N, Priestnall I, Dallin P, Andrews J, Lewis I, Davis K, Owen H, George MW (2010) Measurement of spatial resolution and sensitivity in transmission and backscattering Raman spectroscopy of opaque samples: impact on pharmaceutical quality control and Raman tomography. Appl Spectrosc 64:476–484. doi:10.1366/000370210791211646

22. Matousek P (2007) Raman signal enhancement in deep spectroscopy of turbid media. Appl Spectrosc 61(8):845–854

23. Oelkrug D (1994) Fluorescence spectroscopy in turbid media and tissues. In: Lakowicz JR (ed) Topics in fluorescence spectroscopy, vol 4. Plenum Press, New York, pp 223–253. doi:10.1007/0-306-47060-8_8

24. Allen E (1964) Fluorescent white dyes: calculation of fluorescence from reflectivity values. J Opt Soc Am 54(4):506–514

25. Oelkrug D, Kortüm G (1968) Zur Berechnung der Lumineszenzreabsorption bei pulverförmigen Substanzen. Zeitschrift für Physikalische Chemie NF 58:181–188. doi:10.1524/zpch.1968.58.1_4.181; see also Kortüm G (1969) Reflectance Spectroscopy, Springer, Berlin

26. Fukshansky L, Kazarinova N (1980) Extension of the Kubelka–Munk theory of light propagation in intensely scattering materials to fluorescent media. J Opt Soc Am 70(9):1101–1111

27. Gade R, Kaden U (1990) True luminescence spectra and luminescence quantum yields of molecules adsorbed on light-scattering media. Part 1.—theory. J Chem Soc Chem, Faraday Trans 86(22):3707–3712

28. Oelkrug D, Brun M, Mammel U (1994) Spatial fluorescence profiles in multiple light scattering systems. J Lumin 60–61:422–425. doi:10.1016/0022-2313(94)90181-3

29. Kubelka P (1948) New contributions to the optics of intensely light-scattering materials. Part I. J Opt Soc Am 38(5):448–448

30. Oelkrug D, Brun M, Hubner P, Rebner K, Boldrini B, Kessler RW (2012) Penetration of light into multiple scattering media: model calculations and reflectance experiments. Part II: the radial transfer. Appl Spectrosc 66(8):934–943

31. Koenig JL, Boerio FJ (1969) Raman scattering and band assignments in polytetrafluoroethylene. J Chem Phys 50(7):2823–2829

32. Peacock CJ, Hendra PJ, Willis HA, Cudby MEA (1970) Raman spectrum and vibrational assignment for poly(tetrafluoroethylene). J Chem Soc Inorg Phys Theor 2943–2947

33. Rabolt JF, Fanconi B (1978) Raman scattering from finite polytetrafluoroethylene chains and a highly oriented TFE-HFP copolymer monofilament. Macromolecules 11(4):740–745. doi:10.1021/ma60064a025

34. Legeay G, Coudreuse A, Legeais J-M, Werner L, Bulou A, Buzaré J-Y, Emery J, Silly G (1998) AF fluoropolymer for optical use: spectroscopic and surface energystudies; comparison with other fluoropolymers. Eur Polym J 34(10):1457–1465. doi:10.1016/s0014-3057(97)00289-9

35. Bratescu MA, Saito N, Takai O (2006) Treatment of immobilized collagen on poly(tetrafluoroethylene) nanoporous membrane with plasma. Jpn J Appl Phys, Part 1 45:8352–8357. doi:10.1143/jjap.45.8352